J Mater Sci (2020) 55:2544–2563

Metals & corrosion

Formation of stress- and thermal-induced martensitic nanostructures in a single crystal with phase-dependent elastic properties

Mahdi Javanbakht[1,*] and Mojtaba Adaei[1]

[1] *Department of Mechanical Engineering, Isfahan University of Technology, Isfahan 84156-83111, Iran*

Received: 20 April 2019
Accepted: 23 September 2019
Published online:
1 October 2019

ABSTRACT

In the present paper, the effect of phase-dependent elastic properties on martensitic phase transformations (PTs) in a single crystal is investigated using the phase field approach. The simplest phase dependence of elastic properties is defined by different Young's moduli for austenite (A) and martensite (M), and its effect is investigated for thermal- and stress-induced propagation of an A–M interface. The phase dependence of elastic properties is then included using the quadratic elastic energy with two constants different for A and martensitic variants. The coupled system of phase field and elasticity equations is solved using the nonlinear finite element method, and various examples of PTs are studied. A planar A–M interface propagation is studied under different thermal and mechanical loadings. It is revealed that the effect of phase-dependent elastic properties is more pronounced when thermal strain is included due to the interplay of elastic, transformational and thermal strains. The thermal-induced growth of a martensitic nucleus and the effect of periodic boundary conditions on the nucleus growth are investigated for both phase-independent (PI) and phase-dependent (PD) elastic properties with thermal strain and without it. Martensitic PTs with two variants are studied under different loadings using a one-fourth model and symmetric boundary conditions to reduce the effect of stress concentrations. Martensitic PTs with two variants are also studied in the presence of two circular holes for both the PI and PD elastic properties. This pronounces the significant effect of heterogeneous stress concentration and the size on the PTs. The effect of phase-dependent elastic properties is also studied on twinning in a martensitic grain embedded inside an austenitic matrix under overcooling. The obtained results reveal a significant effect of phase-dependent elastic properties on different types of martensitic PTs and remarkably change the interpretation of structural transformations at the nanoscale.

Address correspondence to E-mail: javanbakht@cc.iut.ac.ir

Springer

https://doi.org/10.1007/s10853-019-04067-6

Introduction

Martensitic phase transformation (PT) is a first-order and displacive transformation which governs several fundamental phenomena such as pseudoelasticity, pseudoplasticity and shape memory effects. During the PTs, austenite and any of the martensitic variants can transform to each other due to mechanical and thermal loadings and change in the surface energy. The crystal symmetry confines the number of possible martensitic variants to three crystallographically equivalent variants for the cubic-to-tetragonal transformation in NiAl. The Ginzburg–Landau (GL) or phase field method (PFM) is broadly used to simulate martensitic PTs at the nanoscale [1–7]. The PFA is also broadly used for the simulation of similar phenomena such as reconstructive PTs [8], twinning [9, 10], dislocations [11–15], melting [16] and fracture [17–20]. It represents an interface between any two neighboring phases with a finite width, which is obtained as the solution of the GL equation. The A–M_i transformation is defined based on an order parameter η_i, which evolution describes the evolution of the ith martensitic variant. The order parameter η_i is an internal variable used to interpolate all material properties between austenite and the ith martensitic variants. Each η_i varies between 0 for austenite to 1 for the ith martensitic variant. The GL equation, which relates the rate of change of η_i linearly to the thermodynamic driving forces or the variational derivatives of the free energy with respect to η_i, describes the PT kinetics. Including stresses requires the coupling of the GL and mechanics. The thermodynamic key advantage of the PFM is that it contains information of all the intermediate states among phases. The order parameters and all the thermomechanical properties continuously vary inside the interface between their values in contacting phases [21]. Also, there is no need to assume the solution geometry [22–33]. The PFM requires a physically defined potential which minima correspond to austenite and martensitic variants and is usually dependent on the order parameters and their gradients, the elastic stress and temperature. Involving any defect such as dislocations and interstitial atoms requires adding some proper terms to the potential. Thus, the GL equations should be coupled to the mechanical equations. In recent decades, various PT phenomena have been studied using the PFM. The equilibrium and stability conditions for PTs were introduced in the PFM in [25, 26], and the corresponding simulations were presented in [29, 31–34]. Surface-induced martensitic PTs were studied based on the FPM in [32, 35, 36]. The effect of interface stresses and large strains on a wide range of stress- and thermal-induced martensitic PTs is discussed in [37–39]. Different types of order parameters such as total strain [23] or transformation strain-related [26] ones have been used in the PFM. Interface widths and energies were investigated in [5]. The interface stress was introduced in [32, 40, 41]. A large-strain-based PFM was performed for martensitic PTs in [34, 41]. Various elastoplastic PFMs were used for martensitic transformation in polycrystalline alloys [42, 43]. A large-strain-based PFM containing the equilibrium and stability conditions was presented in [34]. A review on the phase field modeling of MPTs was presented in [22]. Stressed PTs and transformation-induced buckling were modeled using a large-strain-based PFM [41]. Direct and reverse tetragonal-to-monoclinic PTs in Zr were studied using the PFM [44–46]. Thermodynamically consistent interface stresses were introduced within a PFM [40, 47]. Anisotropy was included in the PFM for plastic-induced PTs in steels [48, 49]. Heterogeneity was also included in the PFM for FCC to BCC transformations in a polycrystalline [50]. A PFM for stress-induced multivariant PTs was developed in [51]. A PFM and 3D FEM were used to simulate beta-to-omega PT in Zr–Nb alloys [52]. A PFM and 2D FEM were used to resolve the nanostructure for Cu–Al–Ni alloy [53]. A PFM was used to resolve internal stresses associated with PTs in Mn–Cu [54]. Square-to-hexagonal transformations were simulated using a PFM [55]. A PFM and the FEM were used for the modeling of bainite–ferrite PTs in TRIP steels [56]. The effect of surface tension and variable surface energy on PTs was studied in NiAl using a PFM in 2D [35]. Different types of martensitic transformations in the presence of defects were studied using the PFM [57–61].

In the present work, the phase field method and the nonlinear finite element method were used to study the effect of phase-dependent elastic properties on martensitic PTs. To do so, the thermal- and stress-induced propagation of a planar A–M interface is studied where the phase dependence of elastic properties is defined by different Young's moduli for different phases. In the next step, the interface propagation is studied under different thermal and mechanical loadings considering the quadratic elastic energy where two elastic constants vary from austenite to martensite. It is revealed that the effect of phase-dependent elastic constants on PTs is more pronounced when the thermal strain is included. Thus, the interplay of elastic, transformational and thermal strains is investigated. The thermal-induced growth of a martensitic nucleus is studied with thermal strain and without it for both phase-independent (PI) and phase-dependent (PD) elastic constants. The effect of periodic boundary conditions (PBCs) on the nucleus growth is also investigated for both the PI and PD elastic constants with thermal strain and without it. Martensitic PTs with two variants are studied under different loadings using a one-fourth model and symmetric boundary conditions to reduce the effect of stress concentrations. Martensitic PTs with two variants are also studied in the presence of two circular holes for both the PI and PD elastic constants. This pronounces the significant effect of heterogeneous stress concentration and the size on the PTs. The effect of PI elastic constants is also studied on twinning in a martensitic grain embedded inside an austenitic matrix under overcooling, and the appearance of triple junctions and twinned nanostructure was investigated under different overcoolings.

System of equations

The Ginzburg–Landau (GL) equation for the evolution of the martensitic variant i is expressed as [31, 35]:

$$\frac{1}{\lambda}\frac{\partial \eta_i}{\partial t} = -\frac{\partial \psi}{\partial \eta_i}\Big|_{\varepsilon_{\mathrm{tot}}} + \nabla\cdot\left(\frac{\partial \psi}{\partial \nabla \eta_i}\right) \tag{1}$$

where λ is the kinetic coefficient. ψ, the Helmholtz free energy per unit volume, consists of the elastic (ψ^{e}), thermal (ψ^{θ}), crystalline $\left(\breve{\psi}\right)$) and gradient ($\psi^{\nabla}$) terms for multivariant martensitic PTs as follows [31, 35]:

$$\psi = \psi^{\mathrm{e}} + \psi^{\theta} + \breve{\psi} + \psi^{\nabla} \tag{2}$$

$$\psi^{\theta} = \frac{1}{2}A_0(\theta-\theta_{\mathrm{e}})\sum_{k=1}^{n}\eta_k^2(3-2\eta_k) - A_0(\theta-\theta_{\mathrm{e}})\sum_{i=1}^{n-1}\sum_{j=i+1}^{n}\eta_i^2\eta_j^2\left(\eta_i+\eta_j\right) \tag{3}$$

$$\begin{aligned}\breve{\psi} = {} & \sum_{k=1}^{n}A_0(\theta_{\mathrm{e}}-\theta_{\mathrm{c}})\eta_k^2(1-\eta_k)^2 + \sum_{i=1}^{n-1}\sum_{j=i+1}^{n}\eta_i\eta_j\left(1-\eta_i-\eta_j\right)\\ & \times\left\{B\left[\left(\eta_i-\eta_j\right)^2-\eta_i-\eta_j\right]+C\eta_i\eta_j\right\}\\ & +\eta_i^2\eta_j^2\left(\eta_i+\eta_j\right)\left(\overline{A}-A_0(\theta_{\mathrm{e}}-\theta_{\mathrm{c}})\right)\end{aligned} \tag{4}$$

$$\psi^{\nabla} = \frac{\beta}{2}\left(\sum_{i=1}^{n}|\nabla\eta_i|^2 + b\sum_{i=1}^{n}\sum_{j=1,i\neq j}^{n}\nabla\eta_i\cdot\nabla\eta_j\right) \tag{5}$$

where A_0 is the energy barrier coefficient for transformation between A and M, θ is temperature, θ_{e} is the equilibrium temperature, θ_{c} is the critical temperature at which stress-free austenite loses its stability to martensite [5, 31, 35], B and C are the energy coefficients for multivariant PTs which affect the energy away from its minima [5, 31, 35], $\overline{A}$ is the energy barrier coefficient between martensitic variants, β is the gradient coefficient which defines the A–M interface and b is the gradient coefficient which defines the M–M interface. The kinetic coefficient and the gradient coefficients are assumed constant. The first derivative in the right side of Eq. (1) is taken at constant strain. The material parameters used in the simulations are listed in Table 1.

The elastic energy is expressed as [31, 35]

$$\psi_{\mathrm{e}} = \frac{1}{2}K\varepsilon_{0\mathrm{e}}^2 + \mu\boldsymbol{E}_{\mathbf{e}} : \boldsymbol{E}_{\mathbf{e}} \tag{6}$$

where K and μ are the bulk and shear moduli, respectively, $\varepsilon_{0\mathrm{e}}$ is the elastic volumetric strain and $\boldsymbol{e}_{\mathbf{e}}$ is the elastic deviatoric strain tensor. In this work, the small strain theory is used. Then, the elastic stress tensor, which is the derivative of the Helmholtz energy per unit volume with respect to the elastic strain tensor, can be written in terms of volumetric and deviatoric strains as [31, 35]:

$$\boldsymbol{\sigma}_{\mathrm{e}} = \frac{\partial \psi_{\mathrm{e}}}{\partial \boldsymbol{E}_{\mathbf{e}}} = K\varepsilon_{0\mathrm{e}}\boldsymbol{I} + 2\mu\boldsymbol{E}_{\mathbf{e}} \tag{7}$$

For the case 1, the Young's modulus varies from austenite to martensite as a function of the phase-order parameter and can be expressed as:

$$\begin{aligned}& E(\eta) = E_{\mathrm{A}} + (E_{\mathrm{M}}-E_{\mathrm{A}})\varphi(\eta) = E_{\mathrm{A}}[1+(n-1)\varphi(\eta)],\\ & \quad \phi(\eta) = \eta^2(3-2\eta)\\ & E_{\mathrm{M}} = nE_{\mathrm{A}}; \quad n = 1, 1.5, 2, 2.5, 3\end{aligned} \tag{8}$$

where n is the ratio of the Young's modulus for

Table 1 Material parameters used in the simulations for NiAl

Parameter	Value	Definition
λ	$2600\ (\mathrm{Pa\ s})^{-1}$	Kinetic coefficient
A_0	$4.4\ \mathrm{MPa\ K^{-1}}$	The energy barrier for transformation between A and M
$\overline{A}$	5.32 GPa	The energy barrier for transformation between martensitic variants
θ_e	215 K	The equilibrium temperature for A and M at stress-free state
θ_c	− 183 K	The critical temperature or A–M stability threshold at stress-free state
B	0	Parameter used for multivariant PTs
C	0.5 GPa	Parameter used for multivariant PTs
β	5.18×10^{-10} N	Gradient coefficient
b	0.5	Gradient coefficient to define M–M interface
K	112.62 GPa	Bulk modulus
μ	71.5 GPa	Shear modulus
γ_A	$1\ \mathrm{J/m^2}$	Surface energy of austenite
γ_M	$0.6\ \mathrm{J/m^2}$	Surface energy of martensite
$C_0^{(1)}$	144 GPa	Elastic constant of austenite
$C_1^{(1)}$	379 GPa	Elastic constant of the first martensitic variant
$C_2^{(1)}$	379 GPa	Elastic constant of the second martensitic variant
$C_0^{(2)}$	74 GPa	Elastic constant of austenite
$C_1^{(2)}$	134 GPa	Elastic constant of the first martensitic variant
$C_2^{(2)}$	134 GPa	Elastic constant of the second martensitic variant
$\boldsymbol{\varepsilon}_{\mathbf{tr1}}$	$\begin{bmatrix} 0.215 & 0 \\ 0 & -0.078 \end{bmatrix}$	Transformational strain tensor for the first martensitic variant
$\boldsymbol{\varepsilon}_{\mathbf{tr2}}$	$\begin{bmatrix} -0.078 & 0 \\ 0 & 0.215 \end{bmatrix}$	Transformational strain tensor for the second martensitic variant
α	$10^{-5}\ \mathrm{K^{-1}}$	Thermal expansion coefficient

martensite to austenite. Substituting Eq. (8) into Eq. (6) gives the elastic energy as

$$\psi_e = E(\eta)\left[\frac{1}{2}\overline{K}\varepsilon_{0e}^2 + \overline{\mu}\boldsymbol{E}_\mathbf{e} : \boldsymbol{E}_\mathbf{e}\right] \quad \overline{K} = \frac{1}{3(1-2v)}$$

$$\overline{\mu} = \frac{1}{2(1+v)}$$

$$\begin{aligned}\overline{\psi}_e &= \frac{1}{2}\overline{K}\varepsilon_{0e}^2 + \overline{\mu}\boldsymbol{E}_\mathbf{e} : \boldsymbol{E}_\mathbf{e} \\ &= \frac{1}{2}\overline{K}\left(\varepsilon_{ex} + \varepsilon_{ey}\right)^2 + \overline{\mu}\left(\varepsilon_{ex}^2 + \varepsilon_{ey}^2 + 2\varepsilon_{exy}^2\right)\end{aligned} \tag{9}$$

Subscript "e" stands for the elastic terms. Taking derivative of Eq. (9) with respect to η and then substituting it into Eq. (1) give the GL equation for a single-order parameter as

$$\begin{aligned}\frac{1}{\lambda}\frac{\partial\eta}{\partial t} &= E_A\left[1 + (n-1)\eta^2(3-2\eta)\right] \\ &\times \left[\left(\overline{K} + 2\overline{\mu}\right)\left[\varepsilon_{ex}\cdot\frac{\partial\varepsilon_{ex}}{\partial\eta} + \varepsilon_{ey}\cdot\frac{\partial\varepsilon_{ey}}{\partial\eta}\right] + \overline{K}\left[\varepsilon_{ex}\cdot\frac{\partial\varepsilon_{ey}}{\partial\eta} + \varepsilon_{ey}\cdot\frac{\partial\varepsilon_{ex}}{\partial\eta}\right]\right. \\ &\left. + 4\overline{\mu}\left[\varepsilon_{exy}\cdot\frac{\partial\varepsilon_{exy}}{\partial\eta}\right]\right] + \left[6E_A(n-1)\eta(1-\eta)\right] \times \left[\frac{1}{2}\overline{K}\left(\varepsilon_{ex} + \varepsilon_{ey}\right)^2\right. \\ &\left. + \overline{\mu}\left(\varepsilon_{ex}^2 + \varepsilon_{ey}^2 + 2\varepsilon_{exy}^2\right)\right] - 2A_0(\theta - \theta_e)\eta(1-\eta) \\ &- A_0(\theta_e - \theta_c)\eta(1-\eta)(1-2\eta) + \beta\nabla^2\eta\end{aligned} \tag{10}$$

On the other hand, the quadratic elastic energy consisting of two martensitic variants is expressed as [41]:

$$\psi_e = 0.5C^{(1)}(\eta_1, \eta_2)(E_1)^2 + C^{(2)}(\eta_1, \eta_2)E_2 \tag{11}$$

where $C^{(1)}$ and $C^{(2)}$ are the functions defining the variation of elastic coefficients among austenite and the first and the second martensitic variants as follows:

$$
\begin{aligned}
C^{(1)}(\eta_1,\eta_2) &= C_0^{(1)} + \left[C_1^{(1)} - C_0^{(1)}\right]\eta_1^2(3-2\eta_1) \\
&\quad + \left[C_2^{(1)} - C_0^{(1)}\right]\eta_2^2(3-2\eta_2) \\
C^{(2)}(\eta_1,\eta_2) &= C_0^{(2)} + \left[C_1^{(2)} - C_0^{(2)}\right]\eta_1^2(3-2\eta_1) \\
&\quad + \left[C_2^{(2)} - C_0^{(2)}\right]\eta_2^2(3-2\eta_2)
\end{aligned} \tag{12}
$$

where $C_0^{(1)}$ and $C_0^{(2)}$ are the elastic constants of austenite; $C_1^{(1)}$ and $C_1^{(2)}$ are the elastic constants of the first martensitic variant; and $C_2^{(1)}$ and $C_2^{(2)}$ are the elastic constants of the second martensitic variant, all of which are obtained by means of the molecular dynamics based on an embedded-atom method [62, 63]. Thus, the elastic potential in Eq. (11) includes the phase dependence of elastic properties for austenite and different martensitic variants.

Also, E_1 and E_2 are the invariants of the elastic strain tensor and can be defined for a plane strain problem as [41]:

$$
\begin{aligned}
E_1 &= \begin{bmatrix} \varepsilon_{xe} & \varepsilon_{xye} \\ \varepsilon_{xye} & \varepsilon_{ye} \end{bmatrix} \sim \begin{bmatrix} 1 & 0 \\ 0 & 1 \end{bmatrix} = \varepsilon_{xe} + \varepsilon_{ye} \\
E_2 &= \begin{bmatrix} \varepsilon_{xe} & \varepsilon_{xye} \\ \varepsilon_{xye} & \varepsilon_{ye} \end{bmatrix} \cdot \begin{bmatrix} \varepsilon_{xe} & \varepsilon_{xye} \\ \varepsilon_{xye} & \varepsilon_{ye} \end{bmatrix} \sim \begin{bmatrix} 1 & 0 \\ 0 & 1 \end{bmatrix} \\
&= \varepsilon_{xe}^2 + \varepsilon_{ye}^2 + 2\varepsilon_{xye}^2
\end{aligned} \tag{13}
$$

The corresponding thermodynamic driving force is proportional to the derivative of the elastic potential with respect to the order parameter. For example, for η_1 it can be expressed as:

$$
\begin{aligned}
\frac{\partial \psi_e}{\partial \eta_1} &= \left(C_1^{(1)} - C_0^{(1)}\right)\frac{\partial \phi(\eta_1)}{\partial \eta_1}\left[\varepsilon_{xe} + \varepsilon_{ye}\right]^2 \\
&\quad + \left(C_0^{(1)} + \left[C_1^{(1)} - C_0^{(1)}\right]\left(\eta_1^2(3-2\eta_1)\right)\right. \\
&\quad \left. + \left[C_2^{(1)} - C_0^{(1)}\right]\left(\eta_2^2(3-2\eta_2)\right)\right)\left[\varepsilon_{xe} + \varepsilon_{ye}\right]\frac{\partial}{\partial \eta_1}\left[\varepsilon_{xe} + \varepsilon_{ye}\right] \\
&\quad + \left(C_1^{(2)} - C_0^{(2)}\right)\frac{\partial \phi(\eta_1)}{\partial \eta_1}\left[\varepsilon_{xe}^2 + \varepsilon_{ye}^2 + 2\varepsilon_{xye}^2\right] \\
&\quad + \left(C_0^{(2)} + \left[C_1^{(2)} - C_0^{(2)}\right]\left(\eta_1^2(3-2\eta_1)\right)\right. \\
&\quad \left. + \left[C_2^{(2)} - C_0^{(2)}\right]\eta_2^2(3-2\eta_2)\right)\frac{\partial}{\partial \eta_1}\left[\varepsilon_{xe}^2 + \varepsilon_{ye}^2 + 2\varepsilon_{xye}^2\right]
\end{aligned} \tag{14}
$$

The total strain tensor $\boldsymbol{\varepsilon}_{\mathbf{tot}}$ in the small strain theory is accepted as the additive decomposition of elastic ($\boldsymbol{\varepsilon}_{\mathbf{e}}$), transformational ($\boldsymbol{\varepsilon}_{\mathbf{tr}}$) and thermal ($\boldsymbol{\varepsilon}_{\boldsymbol{\theta}}$) terms:

$$
\boldsymbol{\varepsilon}_{\mathbf{tot}} = \boldsymbol{\varepsilon}_{\mathbf{e}} + \boldsymbol{\varepsilon}_{\mathbf{tr}} + \boldsymbol{\varepsilon}_{\boldsymbol{\theta}} \tag{15}
$$

The transformational strain tensor with two martensitic variants can be written as:

$$
\boldsymbol{\varepsilon}_{\mathbf{tr}} = \boldsymbol{\varepsilon}_{\mathbf{tr}1}\left(3\eta_1^2 - 2\eta_1^3 - 3\eta_1^3\eta_2^2\right) + \boldsymbol{\varepsilon}_{\mathbf{tr}2}\left(3\eta_2^2 - 2\eta_2^3 - 3\eta_2^3\eta_1^2\right) \tag{16}
$$

The transformational strain tensors for the first and the second martensitic variants are $\boldsymbol{\varepsilon}_{\mathbf{tr}1}$ and $\boldsymbol{\varepsilon}_{\mathbf{tr}2}$, respectively. Assuming the same thermal expansion coefficient for both austenite and martensitic variants [64, 65] gives $\frac{\partial \boldsymbol{\varepsilon}_{\boldsymbol{\theta}}}{\partial \eta_i} = 0$. Taking the derivative of potential with respect to the order parameter at the constant total strain (Eq. 1) gives [31]

$$
\left.\frac{\partial \boldsymbol{\varepsilon}_{\mathbf{e}}}{\partial \eta_i}\right|_{\boldsymbol{\varepsilon}_{\mathbf{tot}}} = -\frac{\partial \boldsymbol{\varepsilon}_{\mathbf{tr}}}{\partial \eta_i} \tag{17}
$$

which for the first and the second variants can be expressed as:

$$
\begin{aligned}
\frac{\partial \boldsymbol{\varepsilon}_{\mathbf{tr}}}{\partial \eta_1} &= 3\eta_1\left(2 - 2\eta_1 - 3\eta_1\eta_2^2\right)\boldsymbol{\varepsilon}_{\mathbf{tr}1} + \left(-6\eta_2^3\eta_1\right)\boldsymbol{\varepsilon}_{\mathbf{tr}2}, \\
\frac{\partial \boldsymbol{\varepsilon}_{\mathbf{tr}}}{\partial \eta_1} &= 3\eta_2\left(2 - 2\eta_2 - 3\eta_2\eta_1^2\right)\boldsymbol{\varepsilon}_{\mathbf{tr}2} + \left(-6\eta_1^3\eta_2\right)\boldsymbol{\varepsilon}_{\mathbf{tr}1}
\end{aligned} \tag{18}
$$

The GL equations for the first and the second variants in a plane strain problem can be expressed as:

$$
\begin{aligned}
\frac{\partial \eta_1}{\partial t} &= -\left\{6\left(C_1^{(1)} - C_0^{(1)}\right)\eta_1(1-\eta_1)\left[\varepsilon_{xe} + \varepsilon_{ye}\right]^2\right. \\
&\quad + \left(C_0^{(1)} + \left[C_1^{(1)} - C_0^{(1)}\right]\eta_1^2(3-2\eta_1)\right. \\
&\quad \left. + \left[C_2^{(1)} - C_0^{(1)}\right]\eta_2^2(3-2\eta_2)\right)\left[\varepsilon_{xe} + \varepsilon_{ye}\right]\frac{\partial}{\partial \eta_1}\left[\varepsilon_{xe} + \varepsilon_{ye}\right] \\
&\quad + 6\left(C_1^{(2)} - C_0^{(2)}\right)\eta_1(1-\eta_1)\left[\varepsilon_{xe}^2 + \varepsilon_{ye}^2 + 2\varepsilon_{xye}^2\right] \\
&\quad + \left(C_0^{(2)} + \left[C_1^{(2)} - C_0^{(2)}\right]\eta_1^2(3-2\eta_1)\right. \\
&\quad \left.\left. + \left[C_2^{(2)} - C_0^{(2)}\right]\eta_2^2(3-2\eta_2)\right)\frac{\partial}{\partial \eta_1}\left[\varepsilon_{xe}^2 + \varepsilon_{ye}^2 + 2\varepsilon_{xye}^2\right]\right\} \\
&\quad - \left\{\frac{1}{3}A_0(\theta - \theta_{\mathrm{e}})\left\{6\eta_1(1-\eta_1) + 2\eta_1\eta_2^2(1.5\eta_1 + \eta_2)\right\}\right. \\
&\quad + \eta_2(1 - \eta_1 - \eta_2)\left\{B(2(\eta_1 - \eta_2) - 1) + D\eta_2\right\} \\
&\quad \left. + 2\eta_1\eta_2^2(1.5\eta_1 + \eta_2)\left(\overline{A} - A_0(\theta_{\mathrm{e}} - \theta_{\mathrm{c}})\right) + \beta\left(\nabla^2\eta_1 + b\nabla^2\eta_2\right)\right\}
\end{aligned}
$$

$$
\begin{aligned}
\frac{\partial \eta_2}{\partial t} = -\Big\{ & 6\left(C_1^{(1)} - C_0^{(1)}\right)\eta_2(1-\eta_2)\left[\varepsilon_{xe} + \varepsilon_{ye}\right]^2 \\
& + \left(C_0^{(1)} + \left[C_1^{(1)} - C_0^{(1)}\right]\eta_2^2(3-2\eta_2)\right. \\
& \left. + \left[C_2^{(1)} - C_0^{(1)}\right]\eta_1^2(3-2\eta_1)\right)\left[\varepsilon_{xe} + \varepsilon_{ye}\right]\frac{\partial}{\partial \eta_2}\left[\varepsilon_{xe} + \varepsilon_{ye}\right] \\
& + 6\left(C_1^{(2)} - C_0^{(2)}\right)\eta_2(1-\eta_2)\left[\varepsilon_{xe}^2 + \varepsilon_{ye}^2 + 2\varepsilon_{xye}^2\right] \\
& + \left(C_0^{(2)} + \left[C_1^{(2)} - C_0^{(2)}\right]\eta_2^2(3-2\eta_2)\right. \\
& \left. + \left[C_2^{(2)} - C_0^{(2)}\right]\eta_1^2(3-2\eta_1)\right)\frac{\partial}{\partial \eta_2}\left[\varepsilon_{xe}^2 + \varepsilon_{ye}^2 + 2\varepsilon_{xye}^2\right]\Big\} \\
& - \Big\{\frac{1}{3}A_0(\theta - \theta_e)\{6\eta_2(1-\eta_2) + 2\eta_2\eta_1^2(1.5\eta_2 + \eta_1)\} \\
& + \eta_1(1-\eta_1-\eta_2)\{B(2(\eta_2-\eta_1)-1) + D\eta_1\} \\
& + 2\eta_2\eta_1^2(1.5\eta_2+\eta_1)\left(\overline{A} - A_0(\theta_e - \theta_c)\right) + \beta\left(\nabla^2\eta_2 + b\nabla^2\eta_1\right)\Big\}
\end{aligned}
\tag{19}
$$

For thermal- and stress-induced PTs, the surface energy is independent of the phase state; thus, the corresponding boundary condition, i.e., insulation boundary condition, can be expressed as [31, 35]:

$$
\beta\left(\nabla\eta_i + b\sum_{j=1, i\neq j}^{n}\nabla\eta_j\right)\cdot \boldsymbol{n} = 0 \tag{20}
$$

To describe the transformation between austenite and one martensitic variant, only one order parameter is needed, i.e., $n = 1$. For example, the insulation boundary condition Eq. (20) reduces to

$$
\beta\nabla\eta_1 \cdot \boldsymbol{n} = 0 \tag{21}
$$

Since there exists only one order parameter, the subscript is usually dropped, i.e., $\beta\nabla\eta\cdot\boldsymbol{n} = 0$.

Numerical simulations

The coupled system of GL and elasticity equations is solved using the nonlinear FEM and the COMSOL Multiphysics code. The GL equations and elasticity equations for martensitic PTs in NiAl are implemented in COMSOL transient diffusion and stationary structural applications, respectively. Triangle Lagrange elements with quadratic approximation for the displacements and order parameters are used. Coupled and segregated options have been used as solvers for the system of equations. Adjustable time steps are used for a better convergence, particularly at the beginning of the solution. During the solving process, automatic mesh refinement is used to avoid mesh inversion-based divergence. The material parameters are used in the simulations as follows [26, 27, 41].

Stress, size and time are normalized by 1 GPa, 1 ps and 1 nm, respectively. The PT thermal driving force is defined by the dimensionless overcooling $\tilde{\theta} = (\theta_e - \theta)/\theta_e$.

To verify the numerical procedure, the interface velocity, energy and width of a planar A–M interface were calculated for thermal-induced and stress-induced PTs and were compared to those of previous studies. To do so, a square sample is considered with the size of 10×10. Half of the sample is initially austenite ($\eta = 0.001$). The other half is initially considered as martensite ($\eta = 0.999$). The sample was initially stress-free. The boundaries are free with the left lower corner fixed in both the x and y directions and the upper left corner fixed in the x direction to avoid rigid body motion. Insulation boundary conditions (Eq. 20) for the phase are applied at all the boundaries which guarantee the constant surface energy over the sample. In order to reduce the internal stress along the y direction and to obtain a vertical interface, the transformation strains for a 36.5° rotated martensite are used as $\boldsymbol{\varepsilon}_{\mathbf{tr}} = \begin{bmatrix} 0.137 & 0.1295 \\ 0.1295 & 0 \end{bmatrix}$ [31]. It is found that for the mesh size smaller than $\delta/6$ (δ is the interface width), the solutions are mesh independent. Here, the largest mesh size is chosen as 0.25. At the equilibrium temperature, the initial sharp A–M interface starts to broaden, creating a diffuse interface. At time t = 0.5, it reaches $\delta = 2.14$ after which δ remains constant (Fig. 1). This value is in a very good agreement with that of an analytical solution ($\delta = 2.04$) for the interface width [4]. The profile of the equilibrated energy function per unit volume along the x direction is plotted in Fig. 2. The interface energy, i.e., the area under the energy profile, is $E_{\text{int}} = 0.2251\ \text{J/m}^2$, which was in a very good agreement with that of an analytical solution ($E_{\text{int}} = 0.2245\ \text{J/m}^2$) for the interface energy [29]. Reducing the temperature increases the PT driving force which causes the interface to start propagation vertically at a constant velocity until the entire sample transforms to the rotated martensite. For a better verification involving stresses, a thermal- and stress-induced PT is considered in a rectangular sample with the size of 20×10. The transformation

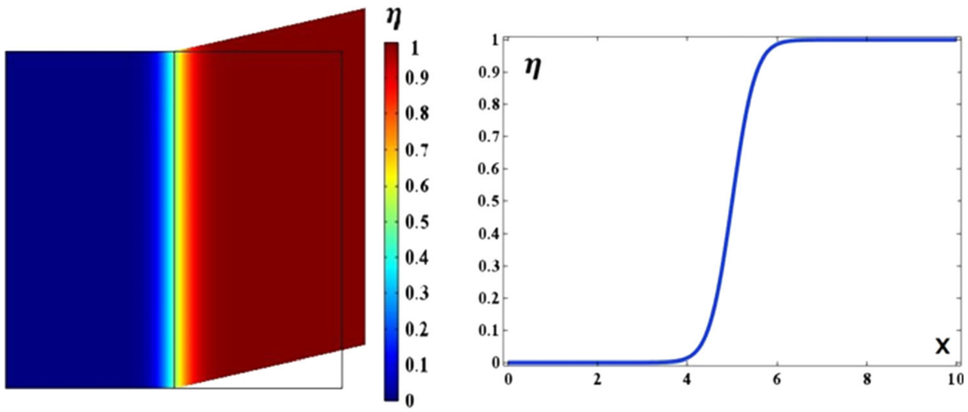

Figure 1 The stationary diffuse A–M interface and its profile along the x direction.

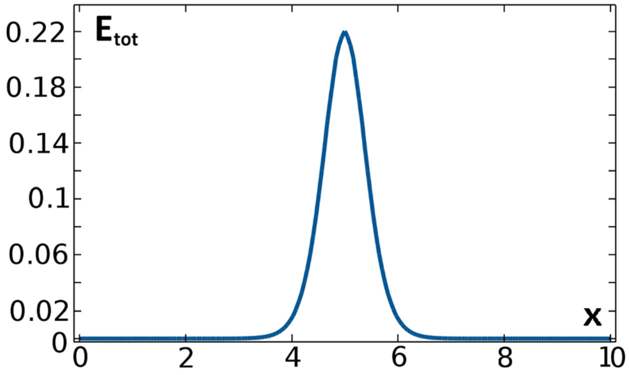

Figure 2 Energy distribution of the equilibrium state along the x direction.

strains are considered as $\boldsymbol{\varepsilon}_{\mathbf{tr}} = \begin{bmatrix} 0.1 & 0 \\ 0 & 0 \end{bmatrix}$. A tensile stress of 0.1 is applied on the right boundary, while the other boundaries are free with the left lower corner fixed in both the x and y directions and the upper left corner fixed in the x direction to avoid rigid body motion. The right boundary of the sample is martensite ($\eta = 0.999$), and the insulation boundary conditions for the phase are applied on the other boundaries. The sample is initially considered as austenite ($\eta = 0.001$). For $\tilde{\theta} = 0.535$ and the applied stress of 0.1, the initial A–M sharp interface first broadens to a diffuse interface and then propagates to the left. For such a condition, the interface width was obtained as $\delta = 2.10$, which was in a very good agreement with the value of $\delta = 2.13$ obtained from an analytical solution [29]. Also, the velocity was obtained as $V = 1072\ \mathrm{m/s}$, which is in a good agreement with the value of $V = 1104\ \mathrm{m/s}$ obtained from an analytical solution [4]. The interface width and velocity remain constant where the stress field is homogeneous and will vary when getting close to the fixed points due to the heterogeneity of stress field. The nanostructure evolution in the deformed state and the corresponding A–M interface profiles are shown in Figs. 3 and 4, respectively.

Effect of phase-dependent (PI) Young's modulus on PTs: the thermal- and stress-induced propagation of an A–M interface

In order to investigate the effect of PI Young's modulus on PTs, the thermal- and stress-induced propagation of an A–M interface is studied in the same sample described in the verification section (Fig. 3). Here, in order to reduce the stress concentration and to avoid divergence due to the mesh inversion, the left side is fixed in the x direction and the lower left corner is fixed in both the x and y directions. The phase dependence of elastic properties is defined by different Young's moduli for different phases. Thus, the parameter $n = E_{\mathrm{M}}/E_{\mathrm{A}}$ is defined and the A–M interface propagation is studied for different values of n and the corresponding interface widths and velocities are plotted in Fig. 5. As can be seen, the interface width is almost independent of n. This could be due to the planar form of the interface as well as neglecting the interface stress effect. For a curved interface, the interface stress creates a local driving force which changes the interface width. The interface velocity linearly increases as n increases. The reason is that increasing n requires a larger stress to move the stiffer interface. Since the velocity linearly depends on the stress [4] and the stress has a linear relation with the Young's modulus, it is reasonable to obtain a linear dependence of the velocity on the coefficient n.

For thermal-induced PTs, i.e., without any applied stress, the elastic heterogeneity did not affect the

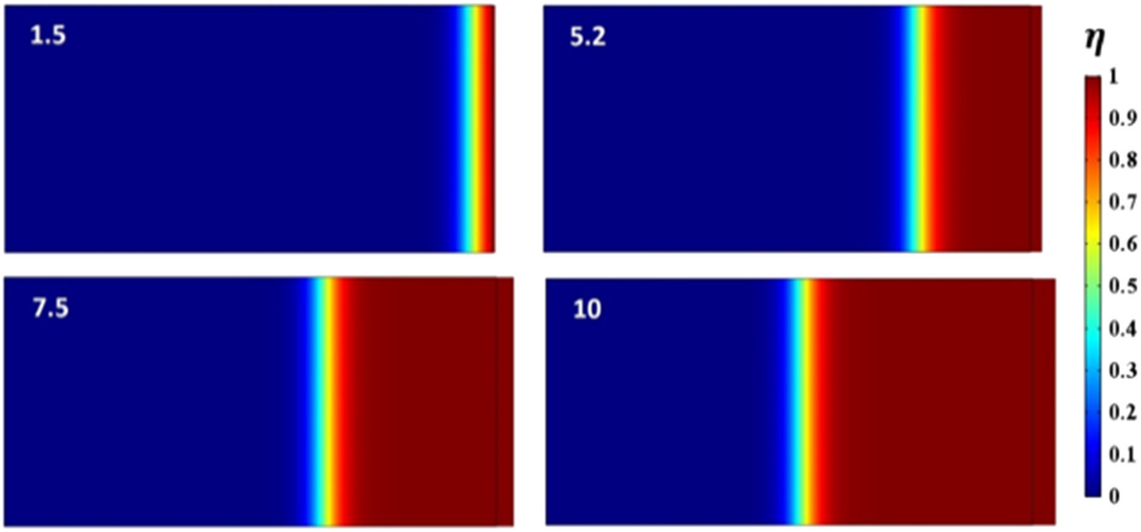

Figure 3 The nanostructure evolution of a thermal- and stress-induced A–M interface propagation.

Figure 4 The evolution of a thermal- and stress-induced A–M interface profile.

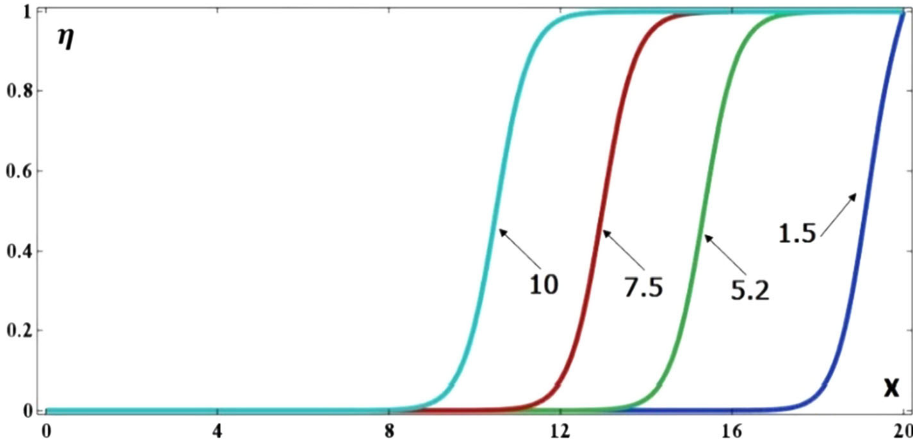

Figure 5 Variation of the A–M interface velocity (V) and width (δ) versus the parameter n.

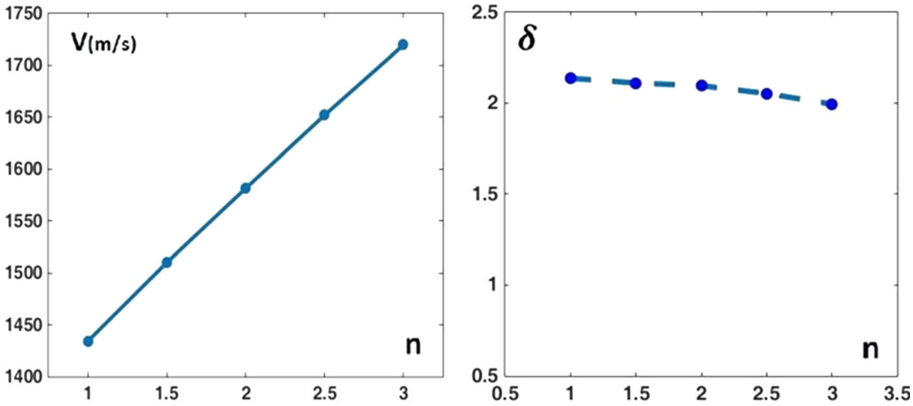

interface width and velocity. The reason is that in the absence of external forces the only stresses available in the material are the internal stresses which are zero here. More importantly, the inelastic interface stress is not considered in this study.

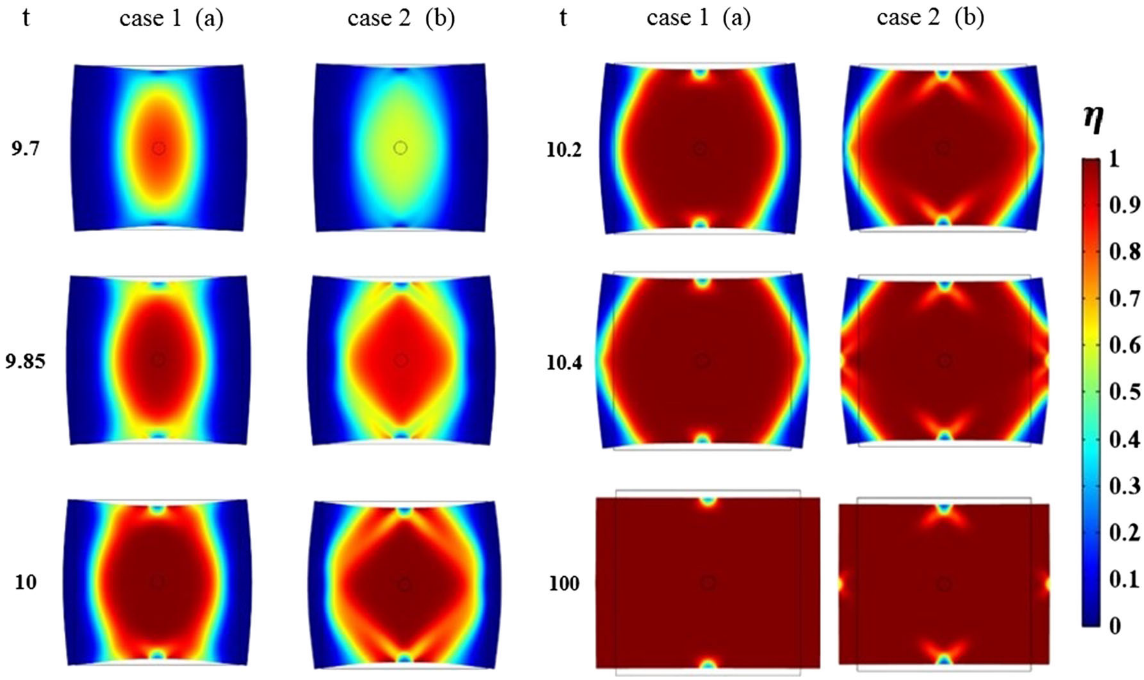

Figure 6 The nucleus growth and nanostructure deformation for the overcooling $\widetilde{\theta} = 1.977$ and the initial value of $\eta = 0.01$ for both the case 1 (**a**) and the case 2 (**b**).

Effect of the quadratic elastic energy with PI constants on the thermal-induced growth of a martensitic nucleus

The thermal-induced growth of a martensitic nucleus is studied with thermal strain and without it with the PI and PD elastic constants. To do so, a square sample with the size of 20×20 is considered in which a circular martensitic nucleus with the radius of 0.75 is considered at its center. The plane strain problem is considered, and the transformation strain of the first martensitic variant is used. The thermal expansion coefficient $\alpha = 10 \times 10^{-6} 1/K$ is considered for both austenite and martensite [64, 65]. All the boundaries are free with two points at the center of the upper and lower sides fixed in the x direction and two points at the center of the lateral sides fixed in the y direction. The nucleus growth and nanostructure deformation for the overcooling $\tilde{\theta} = 1.977$ and the initial value of $\eta = 0.01$ with the PI and PD elastic constants are presented in Fig. 6a, b, respectively. For simplicity, the solution with the PI elastic constants is called case 1 and with the PD elastic constants is called case 2 through the paper. It is found that not only the beginning stages of the growth are not the same but also the transformation paths and the final solutions are different. Moreover, the velocity of the martensitic nanostructure growth is higher for the case 2 than that for the case 1. However, it contains a larger amount of non-complete martensite. The effect of stress concentration due to the fixed points on the PT is remarkable, and it is more pronounced for the case 2. The transformation path is quite different for both cases, the growth velocity is higher for the case 1, and the final solution for the case 1 contains residual austenite near the upper and lower fixed points, while it contains residual austenite and non-complete martensite near all the fixed points for the case 2. One of the main differences between two cases is the appearance of a significant amount of non-complete martensite during transformation for the case 2. This could be more pronounced when the interface stress is included.

Phase concentration here is defined as the ratio of the area of the transformed region to the area of the entire sample. As can be seen in Fig. 7, the phase concentration of the case 2 is larger than that of the case 1 between t = 9.5–11 which belongs to the period where pre-transformation is dominant in the sample (Fig. 6). For the rest of the evolution time, the concentration is very close for two cases.

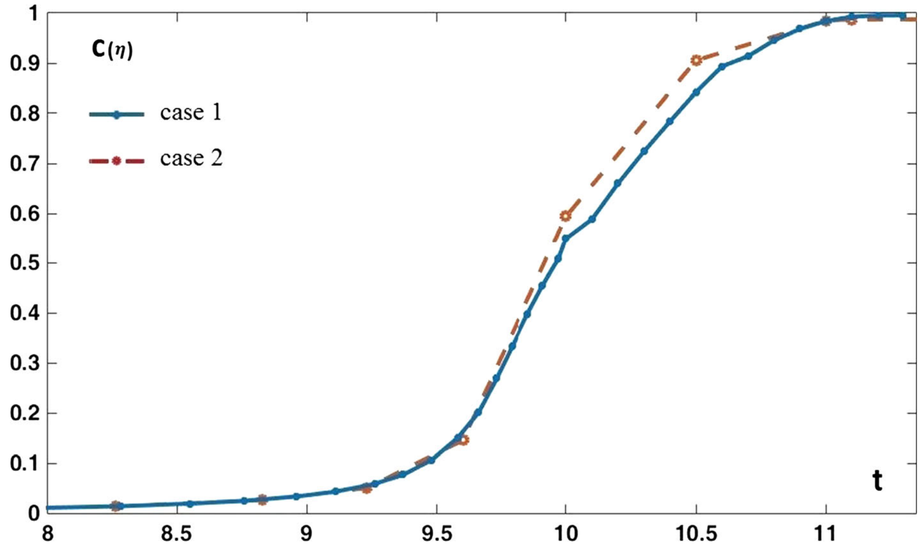

Figure 7 The variation of the phase concentration of the first martensitic variant during time for the overcooling $\widetilde{\theta} = 1.977$ and the initial value of $\eta = 0.01$ for both the cases 1 and 2.

Table 2 The corresponding overcoolings with the thermal strain and without it for both the cases 1 and 2 with PBCs

$\eta_{\text{ini}} = 0.001$ $r = 0.75$	$\tilde{\theta}$			
	Case 1 without PBCs	Case 2 without PBCs	Case 1 with PBCs	Case 2 with PBCs
With thermal strain	1.614	1.456	2.535	4.953
Without thermal strain	2.028	2.033	2.628	5.419

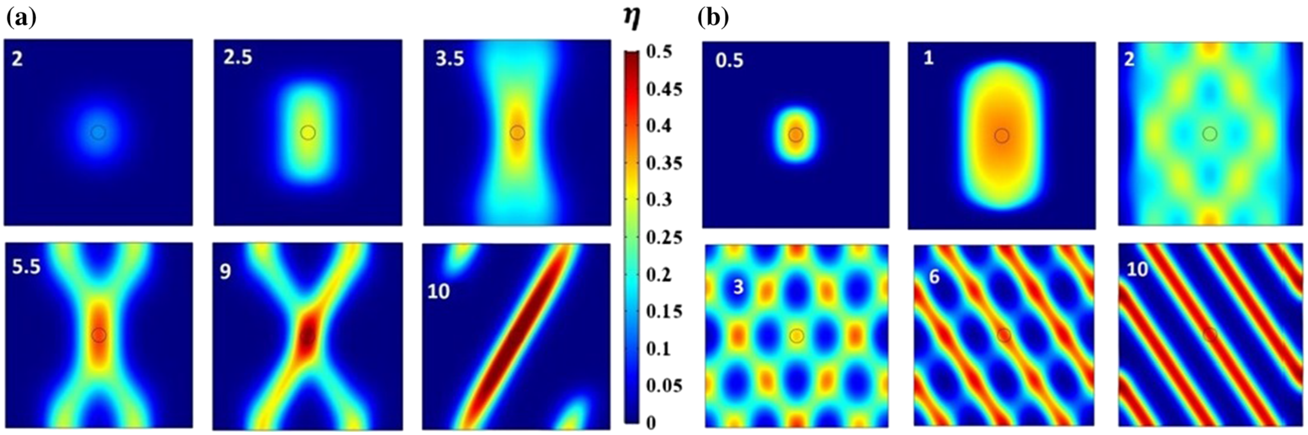

Figure 8 The evolution of nucleus growth for the case 1 (**a**) and the case 2 (**b**) with PBCs.

Effect of periodic boundary conditions on the thermal-induced growth of a martensitic nucleus

In the same problem as in Sect. 3.2, the effect of periodic boundary conditions (PBCs) on the nucleus growth is investigated for both the cases 1 and 2. The PBCs are applied on the boundaries of a square sample with the size of 20 × 20 at the center of which a nucleus with the radius of 0.75 and the initial value of 0.001 are considered. The rest of the sample is initially austenite. The temperature is reduced to find the lowest overcooling at which the nucleus grows. Table 2 presents the overcoolings with thermal strain and without it for both the cases 1 and 2. It is found that the PBCs require a significantly larger

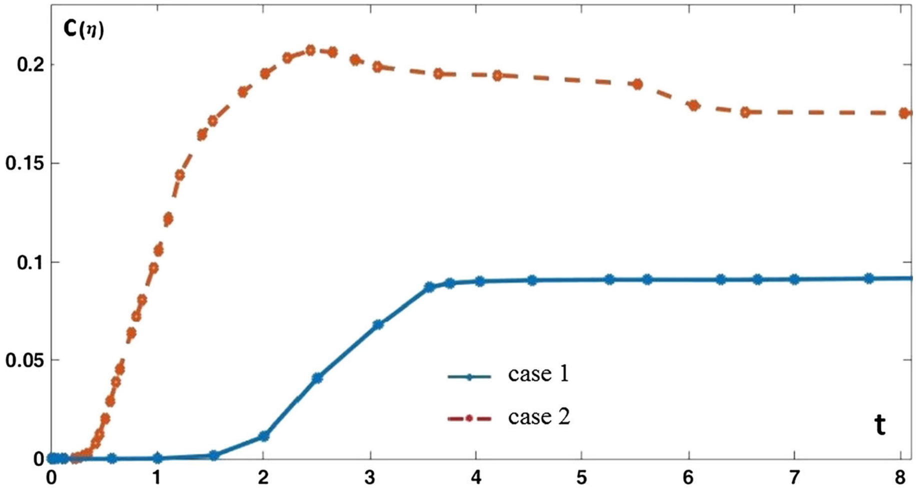

Figure 9 The variation of the phase concentration of the first martensitic variant during time for both the cases 1 and 2 with PBCs.

overcooling to grow the nucleus, and this is more pronounced with the thermal strain. Also, the thermal strain shows a larger effect for the case 2. The evolution of nucleus growth is presented for the cases 1 and 2 in Fig. 8a, b, respectively. Comparing the evolutions shows the nucleus growth path is also completely different than that with the non-PBCs for both the cases. For the case 1 (Fig. 8a), despite the significant growth of the non-complete martensite at the initial stages, a reverse PT occurs and most of the non-complete martensite splits into pieces and transforms back to austenite. The final solution contains an inclined complete martensitic band with some non-complete martensite at the upper and lower boundaries. Therefore, the PBCs minimize the energy of the system in a completely different way. For the case 2 (Fig. 8b), after the non-complete martensite grows and fills the entire sample, the reverse PT occurs and austenite appears in different places creating a periodic pattern of austenite inside a matrix of the non-complete martensite. The final solution contains parallel inclined bands of the non-complete martensite separated by austenite.

The variation of the phase concentration of the first martensitic variant during time is illustrated in Fig. 9. As can be seen, the phase concentration of the case 2 is quite larger than that of the case 1 for any time during evolution.

Thermal- and stress-induced PTs with two martensitic variants under uniaxial stress loading

Martensitic PTs with two variants are studied in a square sample with the size of 27 × 27. To reduce the effect of stress concentration and also to reduce the computational effort, a one-fourth model is used in which the symmetric boundary conditions are applied on the left and lower sides and the upper and the right sides are subjected to the tensile stress of $\widehat{\sigma} = 10$. The plane transformation strain components for the first and the second martensitic variants are considered. A preexisting circular nucleus with the radius size of 2 and the initial values of $\eta_1 = \eta_2 = 0.1$ is considered in the left corner, and the rest of the sample is initially austenite, i.e., $\eta_1 = \eta_2 = 0$. The maximum mesh size is 0.2, which leads to a mesh-independent solution for both triangular and quadrilateral elements. The temperature is $\tilde{\theta} = 1$. For the above conditions, the nucleus for the second variant disappears, while the first variant grows and propagates through the sample until the entire sample is almost transformed to the first variant. This can be explained based on the transformation work. Both the applied stress in the x direction ($\widehat{\sigma_x} = 10$) and the x component of the transformation strain for the first variant ($\varepsilon^x_{\mathrm{tr}1} = 0.215$) are positive. Thus, the corresponding transformation work will be positive. Also, there is no applied stress applied on the vertical sides; thus, it does not contribute to the transformation work for any of the martensitic variants. Therefore, the above transformation works combined together result in a positive transformation work for

Figure 10 The evolution of martensitic nanostructure for the case 1 (**a**) and the case 2 (**b**) under uniaxial stress of $\widehat{\sigma_x} = 10$: one-fourth model.

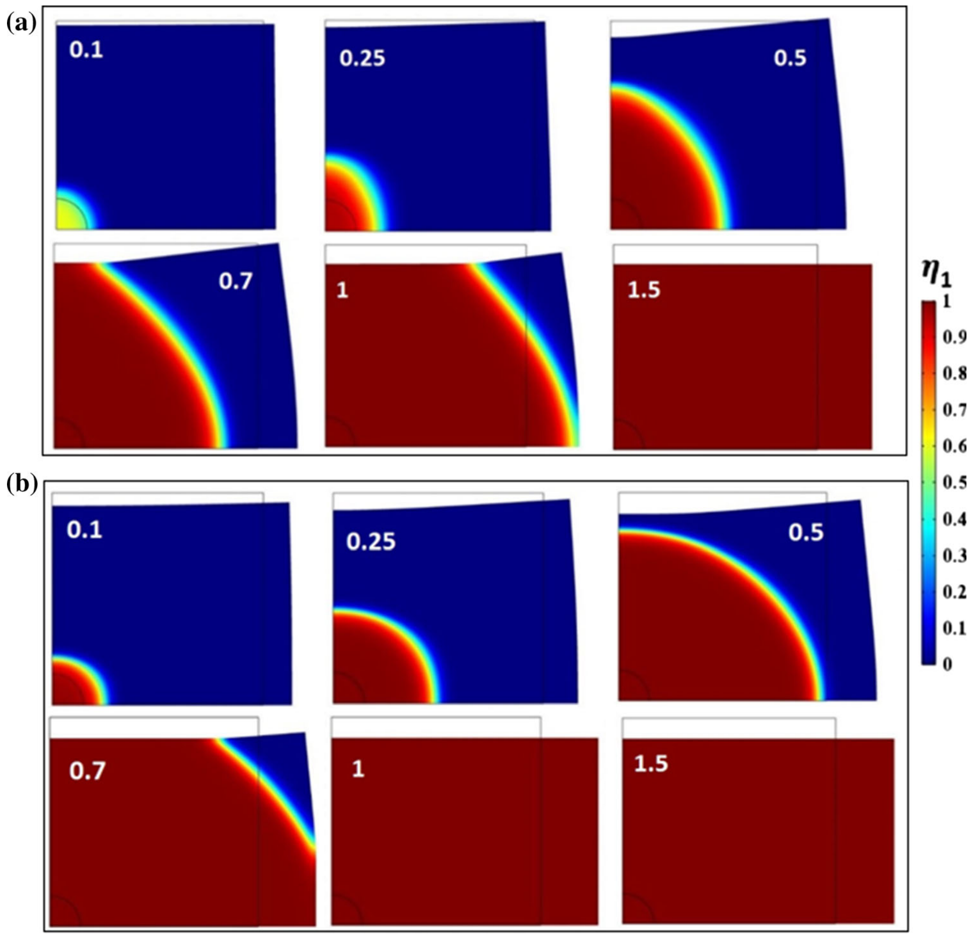

Figure 11 The variation of the phase concentration of the first martensitic variant during time for both the cases 1 and 2 with PBCs.

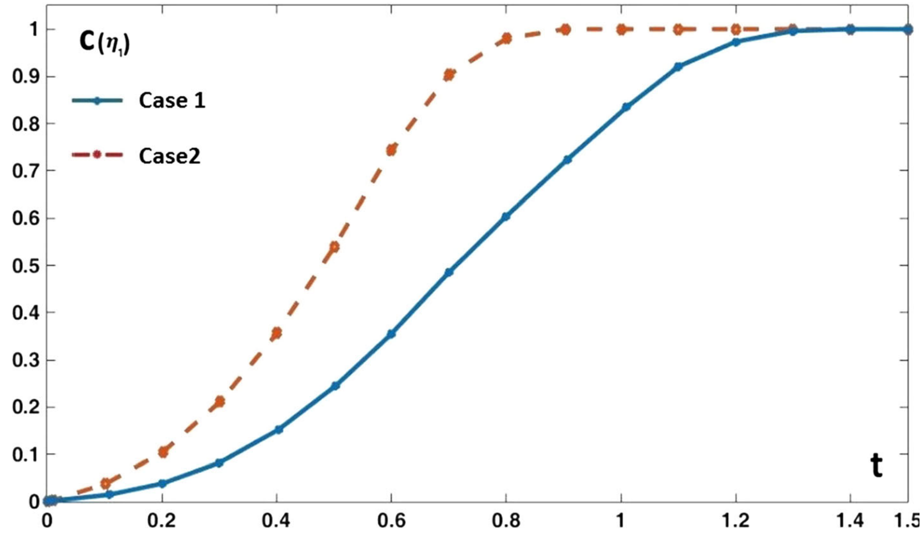

the first variant which promotes the transformation of austenite to the first martensitic variant. On the other hand, since the x component of the transformation strain for the second variant ($\varepsilon^{x}_{\mathrm{tr}2} = -0.078$) is negative, the corresponding transformation work under tensile stress will be negative. Also, no transformation work is provided for the second component of the transformation work due to the lack of applied stress in the y direction. Thus, the total transformation work for the second variant will be negative which suppresses the transformation of austenite to the second martensitic variant. The evolution of martensitic nanostructure is presented for both the cases 1 and 2 in Fig. 10a, b, respectively. For both the cases, only the first variant grows and the second variant disappears. However, for the case 2 the nucleus grows faster and the martensite propagates faster through the sample. Also, the A–M_1 interface width and curvature are different for both the cases. Also, as can be seen in Fig. 11, the phase concentration for the case 2 is quite larger than that for the case 1 for any time during evolution until the stationary solution is reached.

Thermal- and stress-induced PTs with two martensitic variants under biaxial stress loading

The same problem as in Sect. 3.4 is considered, but the upper side is subjected to the tensile stress of $\widehat{\sigma} = 7$ and the left side is subjected to the compressive stress of $\widehat{\sigma} = 7$. Here, the nucleus for the first variant disappears, while the second variant grows and propagates through the sample until the entire sample is almost transformed to the second variant. This can be explained based on the transformation work. The applied stress in the x direction is compressive ($\widehat{\sigma_x} = -7$), while the x component of the transformation strain for the first variant ($\varepsilon^x_{tr1} = 0.215$) is positive. Thus, the corresponding transformation work will be negative. Also, the applied stress in the y direction is tensile ($\widehat{\sigma_x} = 7$), while the y component of the transformation strain for the first variant ($\varepsilon^y_{tr1} = -0.078$) is negative. This also gives a negative transformation work for the first variant. The above transformation works combined together result in a negative transformation work for the first variant which suppresses the transformation of austenite to the first martensitic variant. On the other hand, both the applied stress in the x direction ($\widehat{\sigma_y} = -7$) and the x component of the transformation strain for the second variant ($\varepsilon^x_{tr2} = -0.078$) are negative, which result in a positive transformation work. Also, both the applied stress in the y direction ($\widehat{\sigma_y} = 7$) and the y component of the transformation strain for the second variant ($\varepsilon^y_{tr2} = 0.215$) are positive, which also result in a positive transformation work. The above transformation works combined together result in a positive transformation work for the second variant which promotes the transformation of austenite to the second martensitic variant. The evolution of martensitic nanostructure is presented in Fig. 12a, b for both the cases 1 and 2, respectively. For both the cases, only the second variant grows and the first variant disappears. However, for the case 2, the nucleus grows faster and the martensite propagates faster through the sample. Also, the A–M_2 interface width and curvature are different for both the cases. Again, as can be seen in Fig. 13, the phase concentration for the case 2 is quite larger than that of the case 1 for any time during evolution until the stationary solution is reached. From the computational point of view, the one-fourth problem can be solved 4–5 times faster than the full geometry model. Also, the convergence was obtained easier and there was no need to use the automatic remeshing which is essential for problems in which mesh inversion occurs due to fixed point boundary conditions.

Thermal- and stress-induced PTs with two martensitic variants in the presence of two holes under biaxial stress loading

Martensitic PTs with two variants are studied in a square sample with the size of 23.3×23.3 with two symmetric circular holes with the radius of 2.66 (located along the horizontal axis) and a distance between the holes of 8. The upper and the lower sides are subjected to the tensile normal stress of $\widehat{\sigma} = 12$, and the lateral sides are subjected to the tensile normal stress of $\widehat{\sigma} = 9$. To avoid rigid body motion, the middle points of the upper and lower sides are fixed in the x direction and the middle points of the lateral sides are fixed in the y direction. The plane transformation strain components for the first and the second martensitic variants are considered. The initial conditions of $\eta_1 = \eta_2 = 0.1$ were prescribed in the rings of radius 3.33 around each hole, and the rest of the sample is initially austenite, i.e., $\eta_1 = \eta_2 = 0$. The mesh map is quite heterogeneous, but it was chosen fine enough with the maximum mesh size of 0.4 to obtain mesh-independent solutions. The temperature is $\tilde{\theta} = 1$. Due to the presence of two holes and small sizes, the stress concentration will play an important role. The evolution of martensitic nanostructure is presented in Figs. 14, 15 for the cases 1 and 2, respectively. The first martensitic variant grows from the space between the holes in the x direction and then grows from the other sides of the hole surfaces

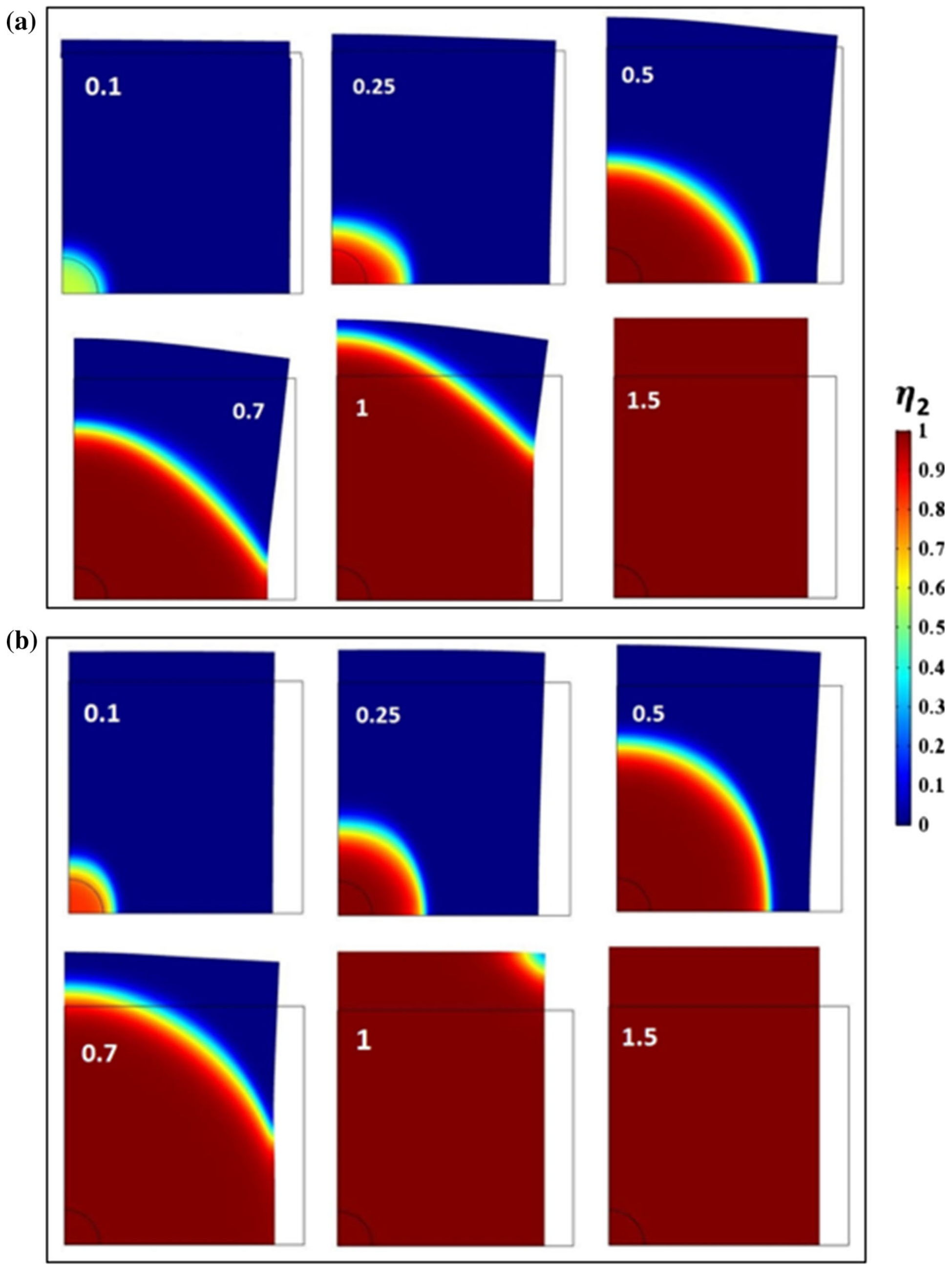

Figure 12 The evolution of martensitic nanostructure for the case 1 (**a**) and the case 2 (**b**) under biaxial stresses of $\widehat{\sigma_x} = -7$ and $\widehat{\sigma_y} = 7$: one-fourth model.

in the x direction. This is expected due to the high stress concentration in the distance between the two holes. Due to the small distance, a pre-transformation occurs in this region due to which the non-complete phase fills the region and then it transforms to the complete phase; thus, a complete interface does not appear at the first stages. The first martensitic variant grows until it reaches the lateral sides and the M_1–M_2 interface remains almost horizontally everywhere. This is because both the applied stress and the transformation strain component of the first variant are positive in the x direction, which lead to a positive transformation work, and this promotes the PT for the first variant. In the following, the M_1–M_2 interface gradually rotates to 45°, and the first variant is surrounded by the M_1–M_2 interface. There also exist small regions of the second variant near the fixed points due to the stress concentration. A larger distance between the holes would allow change in the orientation of the M_1–M_2 interface. The second martensitic variant grows vertically from the holes surfaces, and the second variant does not appear in

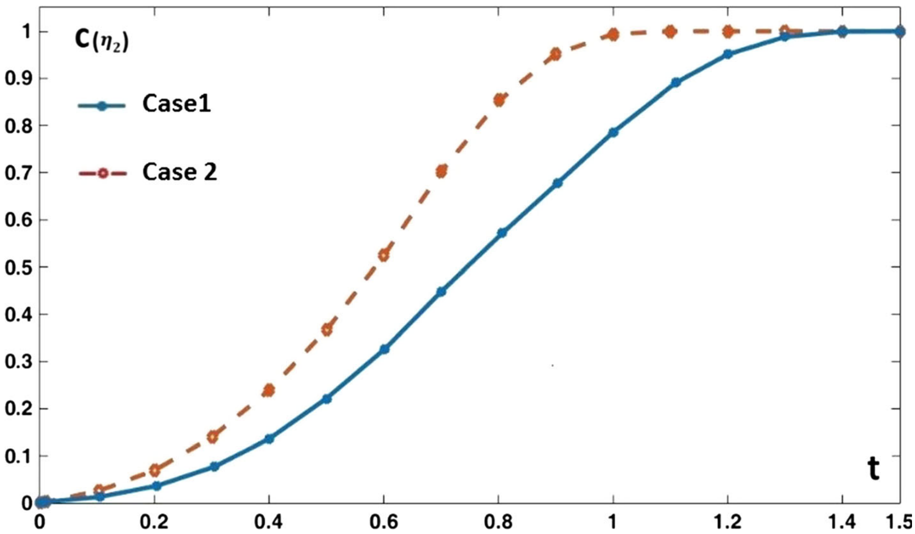

Figure 13 The variation of the phase concentration of the second martensitic variant during time for both the cases 1 and 2 under biaxial stresses of $\widehat{\sigma_x} = -7$ and $\widehat{\sigma_y} = 7$.

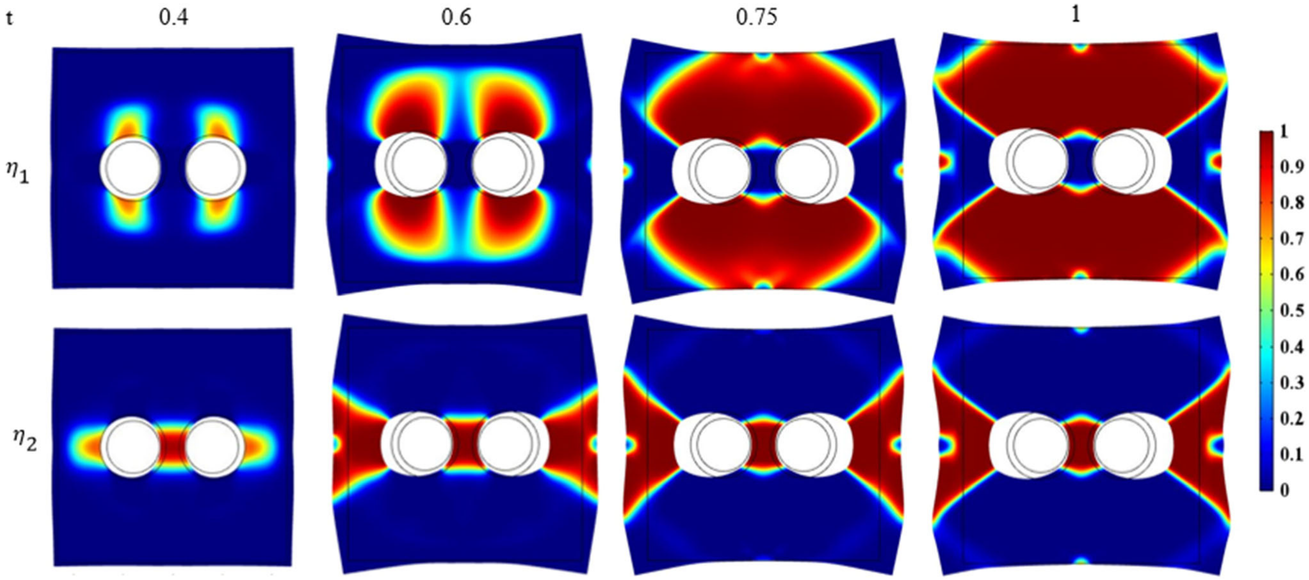

Figure 14 The evolution of the nanostructure for both martensitic variants η_1 and η_2 for the case 1 under biaxial stresses of $\widehat{\sigma_x} = 12$ and $\widehat{\sigma_y} = 9$.

the distance between the holes. This is because the applied stress in the x direction is positive, while the transformation strain component of the second variant in the x direction is negative ($\varepsilon^x_{tr2} = -0.078$), and this leads to a negative transformation work which suppresses the PT of the second variant. The second variant nanostructure grows vertically until it reaches the upper and lower sides. During the evolution, the frontier part of the transformed region is an A–M$_2$ interface with a variable width at different places, which largest size belongs to the place where the two frontiers of the transformed regions (of the second variant) coalesce. On the other hand, a M$_1$–M$_2$ interface is created at the boundary of the transformed region starting from the hole surface which progresses along the 45° direction and is stopped near the corner. This interface surrounds the lower band of the transformed region of the second variant. A region of residual austenite remains near the corner; thus, an A–M$_2$ interface is created, separating residual austenite from the second variant region. Note that the A–M$_2$ interface width is larger than that of the M$_1$–M$_2$ interface. Compared to the case 1, for the case 2 the transformed region propagates faster until the stationary solution is reached, there exists a remarkable amount of non-complete first and second

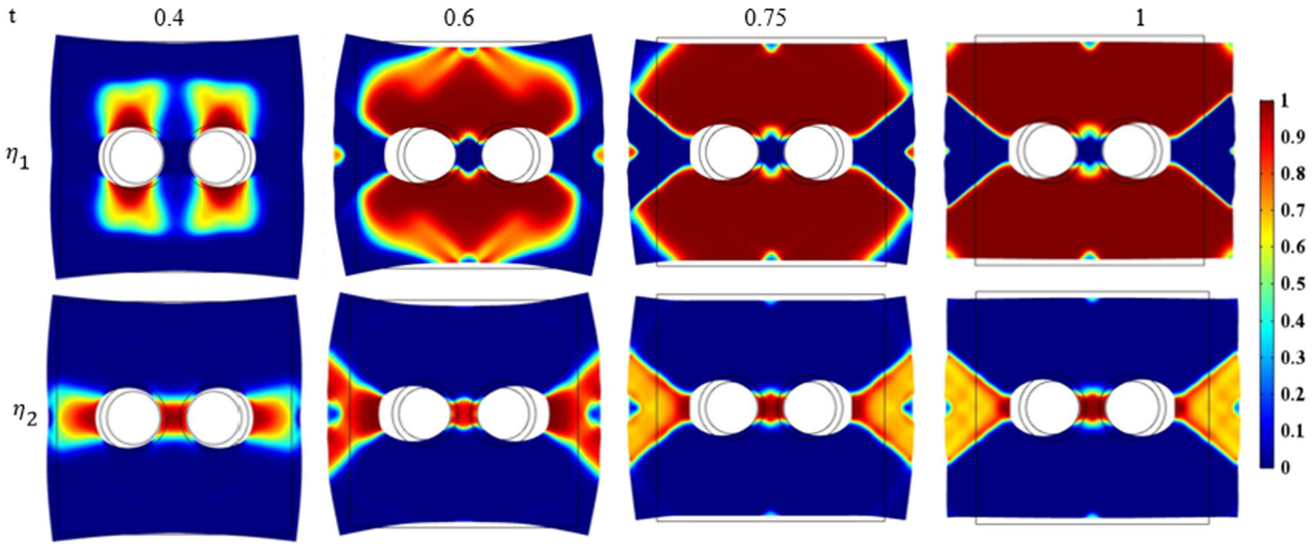

Figure 15 The evolution of the nanostructure for both martensitic variants η_1 and η_2 for the case 2 under biaxial stresses of $\widehat{\sigma_x} = 12$ and $\widehat{\sigma_y} = 9$.

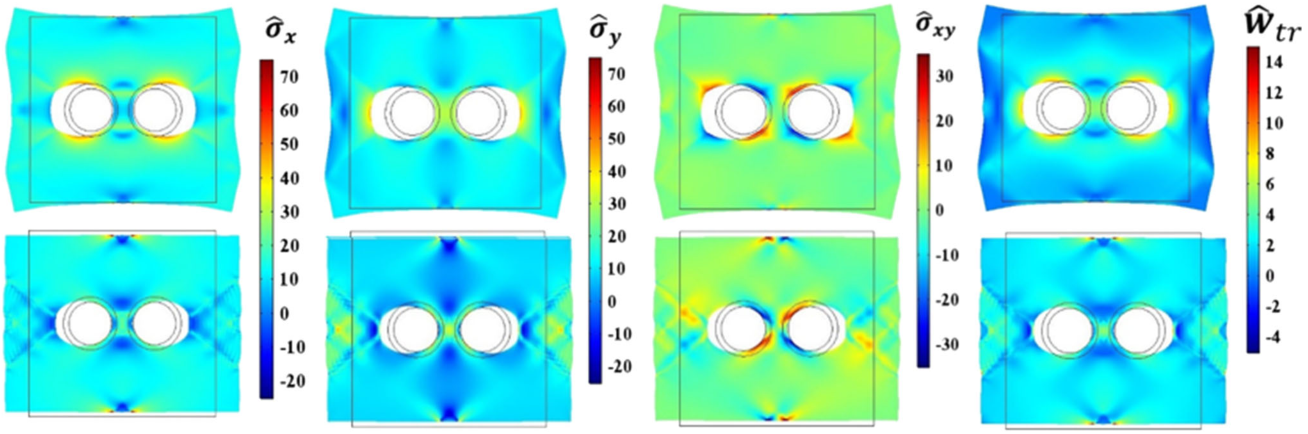

Figure 16 The distribution of stress components and the transformation work $\widehat{W_{xy}}$ of the stationary solution for the case 1 (the top row) and the case 2 (the bottom row) under biaxial stresses of $\widehat{\sigma_x} = 12$ and $\widehat{\sigma_y} = 9$.

martensitic variants during the propagation, and in the stationary solution, there is no residual austenite at the corners and the M_1–M_2 interface is thinner. Also, the stress concentration due to the fixed points shows a more significant effect on the PT, creating a more complex morphology. Figure 16 shows the distribution of stress components $\widehat{\sigma_x}$, $\widehat{\sigma_y}$ and $\widehat{\sigma_{xy}}$ and the transformation work $\widehat{W_{xy}}$ of the stationary solution for both the cases. As can be seen, there exists a remarkable difference between the stresses and also the transformation work of both the cases, which leads to a big difference in the transformation event of both the cases.

Thermal-induced twinning in a nanograin embedded in an austenitic square matrix

Thermal-induced phase transformations with the PI elastic constants (case 1) and the PD elastic constants (case 2) are studied inside a nanograin with the size of 12.5 × 12.5 embedded at the center of an austenitic square matrix with the size of 50 × 50 (Fig. 17a). The lower left corner is fixed in both the x and y directions, and the upper left corner is fixed in the x direction. The insulation boundary condition is applied on all the boundaries for the phase field problem. The initial condition for the nanograin is $\eta_1 = \eta_2 = 0.99$ for a fast convergence. The rest of the

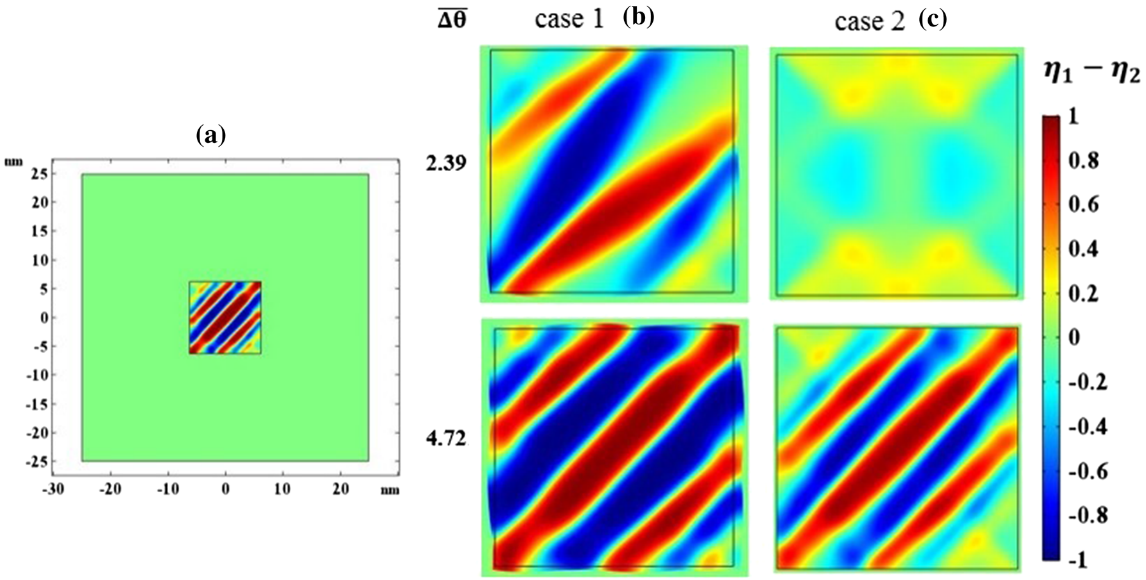

Figure 17 Schematics of a martensitic nanograin embedded in at the center of an austenitic square matrix (**a**), the martensitic nanostructure for the case 1 (**b**) and the case 2 (**c**).

sample is kept during the solution in the austenitic condition, i.e., $\eta_1 = 0$. The problem is solved for t = 100 to reach the stationary solution. Under such a condition and with no mechanical loadings and no stress concentration, the problem is almost thermal induced. Our interest is to obtain twinned structures for both the cases which can be obtained under large overcoolings when no stress exists. Thus, the temperature was reduced to find the twinned structure. The martensitic nanostructure is presented in Fig. 17 for two different overcoolings of 2.39 and 4.72. For the lower overcooling of 2.39, no twinned structure is resolved for either case 1 or 2. For the case 1 (Fig. 17b), several complete and non-complete bands of the first and the second variants (particularly near the boundaries due to the space limitation and the insulation boundary conditions) appear which are separated by austenite, creating triple junctions of three phases, while for the case 2 (Fig. 17c), no martensite appears for the same overcooling. Also, the orientation of the possible martensitic nanostructure looks different. For the larger overcooling of 4.72, for both the cases the twinned structure appears. Due to the small size and insulation boundary conditions, the martensitic ribbons have variable thicknesses and the A–M and the M–M interface widths are variable. Also, small junctions of the three phases exist at the boundary.

Conclusion

In this paper, the phase field and the nonlinear finite element methods were used to study the effect of phase-dependent elastic properties on martensitic PTs. The phase dependence of elastic properties was defined by different Young's moduli for austenite and martensite, and its effect was investigated on thermal- and stress-induced propagation of an A–M interface. It was found that as the difference between the Young's moduli of A and M increases, the A–M interface velocity linearly increases. However, the interface width decreases very little. The phase dependence of elastic properties was then included using the quadratic elastic energy in which two constants are different for A and martensitic variants. A planar A–M interface propagation was studied under different thermal and mechanical loadings. It was revealed that the effect of phase-dependent elastic properties is more pronounced when thermal strain is included, resulting in a larger interface velocity. The promoting effect of the thermal strain decreased as the applied stress was increased. The thermal-induced growth of a martensitic nucleus and the effect of PBCs on the nucleus growth were investigated for both the PI (case 1) and PD (case 2) elastic properties with thermal strain and without it. The effect of the PD elastic properties was more pronounced in the presence of stress concentration. The transformation path, the growth velocity and the final solutions were different for the cases 1 and 2. It was found that the PBCs require a significantly larger overcooling for the nucleus growth, particularly with thermal strain and for the case 2. The nucleus growth path was also completely different than that with the non-PBCs for both the cases 1 and 2. Martensitic PTs with two variants were studied under different loadings using a one-fourth model and symmetric boundary conditions to reduce the effect of stress concentrations. Martensitic PTs with two variants were also studied in the presence of two circular holes. Due to the stress concentration, the martensite grows first near the holes. It also resulted in residual austenite inside the other phases. Compared to the case 1, the transformed region for the case 2 propagated faster for the initial stages and there existed a remarkable amount of non-complete martensite during evolution. Also, pre-transformation occurred in the small distance between the two holes and a non-complete phase fills the region which later transforms to the complete phase. The effect of phase-dependent elastic properties was also studied on twinning in a martensitic grain embedded inside austenite. Under lower overcoolings, no twinned structure was resolved for either case. Instead, for the case 1, several bands of the first and the second variants appeared separated by austenite, creating triple junctions of three phases, while for the case 2 no martensite appeared. For larger overcoolings, for both the cases the twinned structure appeared. The obtained results show the significant effect of phase-dependent elastic properties on martensitic PTs. Similarly, the same effect would be predicted for other similar phenomena such as reconstructive PTs, diffusion and defect dynamics.

Acknowledgements

The help of Isfahan University of Technology is gratefully acknowledged.

Compliance with ethical standards

Conflict of interest The authors declare that they have no conflict of interest.

References

[1] Jacobs AE, Curnoe SH, Desai RC (2003) Simulations of cubic-tetragonal ferroelastics. Phys Rev B 68:224104

[2] Jin YM, Artemev A, Khachaturyan AG (2001) Three-dimensional phase field model of proper martensitic transformation. Acta Mater 49:2309–2320

[3] Chen LQ (2002) Phase-field models for microstructure evolution. Annu Rev Mater Res 32:113–140

[4] Levitas VI, Lee DW, Preston DL (2010) Interface propagation and microstructure evolution in phase field models of stress-induced martensitic phase transformations. Int J Plasticity 26:395–422

[5] Levitas VI, Javanbakht M (2011) Phase-field approach to martensitic phase transformations: effect of martensite–martensite interface energy. Int J Mater Res 102:652–665

[6] Seol DJ, Hu SY, Li YL, Chen LQ, Oh KH (2003) Cubic to tetragonal martensitic transformation in a thin film elastically constrained by a substrate. Met Mater Int 9:221–226

[7] Rasmussen KO, Lookman T, Saxena A, Bishop AR, Albers RC, Shenoy SR (2001) Three-dimensional elastic compatibility and varieties of twins in martensites. Phys Rev Lett 87:055704

[8] Denoual C, Caucci AM, Soulard L, Pellegrini YP (2010) Phase-field reaction-pathway kinetics of martensitic transformations in a model Fe3Ni alloy. Phys Rev Lett 105:035703

[9] Clayton JD, Knap J (2011) A phase field model of deformation twinning: nonlinear theory and numerical simulations. Phys D 240:841–858

[10] Levitas VI, Roy AM, Preston DL (2013) Multiple twinning and variant-variant transformations in martensite: phase-field approach. Phys Rev B 88:054113

[11] Wang YU, Jin YM, Khachaturyan AG (2003) Phase field microelasticity modeling of dislocation dynamics near free surface and in heteroepitaxial thin films. Acta Mater 51:4209–4223

[12] Hu SY, Li YL, Zheng YX, Chen LQ (2004) Effect of solutes on dislocation motion: a phase-field simulation. Int J Plast 20:403–425

[13] Rodney D, LeBouar Y, Finel A (2003) Phase field methods and dislocations. Acta Mater 51:17–30

[14] Wang YU, Li J (2010) Phase field modeling of defects and deformation. Acta Mater 58:1212–1235

[15] Levitas VI, Javanbakht M (2012) Advanced phase field approach to dislocation evolution. Phys Rev B 86:140101

[16] Slutsker J, Thornton K, Roytburd AL, Warren JA, McFadden GB (2006) Phase field modeling of solidification under stress. Phys Rev B 74:014103

[17] Farrahi GH, Javanbakht M, Jafarzadeh H (2018) Phase field modeling of crack growth and analytical treatment on the parameters. Contin Mech Therm. https://doi.org/10.1007/s00161-018-0685-z

[18] Levitas VI, Jafarzadeh H, Farrahi GH, Javanbakht M (2018) Thermodynamically consistent and scale-dependent phase field approach for crack propagation allowing for surface stresses. Int J Plast 111:1–35

[19] Farrahi GH, Javanbakht M, Jafarzadeh H (2018) Phase field modeling of crack growth and analytical treatment on the parameters. Contin Mech Therm. https://doi.org/10.1007/s00161-018-0685-z

[20] Msekh MA, Silani M, Jamshidian M, Areias PM, Zhuang X, Zhuang X, Zi G (2016) Predictions of J integral and tensile strength of clay/epoxy nanocomposites material using phase field model. Compos Part B Eng 93:97–114

[21] Levitas VI, Warren JA (2016) Phase field approach with anisotropic interface energy and interface stresses: large strain formulation. J Mech Phys Solids 91:94–125

[22] Mamivand M, Asle Zaeem M, Hel Kadiri (2013) A review on phase field modeling of martensitic phase transformation. Comp Mater Sci 77:304–311

[23] Finel A, Bouar YL, Gaubert A, Salman U (2010) Phase field methods: microstructures, mechanical properties and complexity. C R Phys 11:245–256

[24] Artemev A, Jin Y, Khachaturyan AG (2001) Three-dimensional phase field model of proper martensitic transformation. Acta Mater 49(7):1165–1177

[25] Levitas VI, Preston DL (2002) Three-dimensional Landau theory for multivariant stress-induced martensitic phase transformations. I. Austenite-martensite. Phys Rev B 66:134206

[26] Levitas VI, Preston DL (2002) Three-dimensional Landau theory for multivariant stress induced martensitic phase transformations. II. Multivariant phase transformations and stress space analysis. Phys Rev B 66:134207

[27] Levitas VI, Preston DL, Lee DW (2003) Three-dimensional Landau theory for multivariant stress-induced martensitic phase transformations. III. Alternative potentials, critical nuclei, kink solutions, and dislocation theory. Phys Rev B 68:134201

[28] Hu SY, Henager CH, Chen LQ (2010) Simulations of stress-induced twinning and de-twinning: a phase field model. Acta Mater 58:6554–6564

[29] Levitas VI, Lee DW (2007) Athermal resistance to interface motion in the phase-field theory of microstructure evolution. Phys Rev Lett 99:245701

[30] Zhang W, Jin YM, Khachaturyan AG (2007) Phase field microelasticity modeling of heterogeneous nucleation and growth in martensitic alloys. Acta Mater 49:565–574

[31] Levitas VI, Javanbakht M (2010) Surface tension and energy in multivariant martensitic transformations: phase-field theory, simulations, and model of coherent interface. Phys Rev Lett 105:165701

[32] Levitas VI, Javanbakht M (2011) Surface-induced phase transformations: multiple scale and mechanics effects and morphological transitions. Phys Rev Lett 107:175701

[33] Levitas VI, Levin VA, Zingerman KM, Freiman EI (2009) Displacive phase transitions at large strains: phase-field theory and simulations. Phys Rev Lett 103:025702

[34] Levitas VI (2013) Phase-field theory for martensitic phase transformations at large strains. Int J Plast 49:85–118

[35] Javanbakht M, Barati E (2016) Martensitic phase transformations in shape memory alloy: phase field modeling with surface tension effect. Comp Mater Sci 115:137–144

[36] Mirzakhani S, Javanbakht M (2018) Phase field-elasticity analysis of austenite–martensite phase transformation at the nanoscale: finite element modeling. Comput Mater Sci 154:41–52

[37] De Suvranu (2017) A phase-field model for shock-induced α-γ phase transition of RDX. Int J Plast 88:140–158

[38] Schoof E, Schneider D, Streichhan N, Mittnacht T, Selzer M, Nestler B (2018) Multiphase-field modeling of martensitic phase transformation in a dual-phase microstructure. Int J Solids Struct 134:181–194

[39] Segawa M, Yamanaka A, Nomoto S (2017) Multi-phase-field simulation of cyclic phase transformation in Fe-C-Mn and Fe-C-Mn-Si alloys. Comp Mater Sci 136:67–75

[40] Levitas VI (2014) Phase field approach to martensitic phase transformations with large strains and interface stresses. J Mech Phys Solids 70:154–189

[41] Levin VA, Levitas VI, Zingerman KM, Freiman EI (2013) Phase-field simulation of stress-induced martensitic phase transformations at large strains. Int J Solids Struct 50:2914–2928

[42] Yamanaka A, Takaki T, Tomita Y (2010) Elastoplastic phase-field simulation of martensitic transformation with plastic deformation in polycrystal. Int J Mech Sci 55:245–250

[43] Kundin J, Raabe D, Emmerich H (2011) A phase-field model for incoherent martensitic transformations including plastic accommodation processes in the austenite. J Mech Phys Solids 59:2082–2102

[44] Mamivand M, Zaeem MA, Kadiri HE, Chen LQ (2013) Phase field modeling of the tetragonal-to-monoclinic phase transformation in zirconia. Acta Mater 61:5223–5235

[45] Mamivand M, Zaeem MA, Kadiri HE (2014) Shape memory effect and pseudoelasticity behavior in tetragonal zirconia polycrystals: a phase field study. Int J Plast 60:71–86

[46] Mamivand M, Zaeem MA, Kadiri HE (2014) Phase field modeling of stress-induced tetragonal-to-monoclinic transformation in zirconia and its effect on transformation toughening. Acta Mater 64:208–219

[47] Levitas VI (2013) Thermodynamically consistent phase field approach to phase transformations with interface stresses. Acta Mater 61:4305–4319

[48] Yeddu HK, Borgenstam A, Agren J (2013) Stress-assisted martensitic transformations in steels: a 3-D phase-field study. Acta Mater 61:2595–2606

[49] Malik A, Amberg G, Borgenstam A, Agren J (2013) Effect of external loading on the martensitic transformation–A phase field study. Acta Mater 61:7868–7880

[50] Heo TW, Chen LQ (2014) Phase-field modeling of displacive phase transformations in elastically anisotropic and inhomogeneous polycrystals. Acta Mater 76:68–81

[51] Momeni K, Levitas VI (2015) A phase-field approach to solid–solid phase transformations via intermediate interfacial phases under stress tensor. Int J Solids Struct 71:39–56

[52] Yeddu HK, Lookman T (2015) Phase-field modeling of the beta to omega phase transformation in Zr–Nb alloys. Mater Sci Eng A 634:46–54

[53] Tuma K, Stupkiewicz S, Petryk H (2016) Size effects in martensitic microstructures: finite-strain phase field model versus sharp-interface approach. J Mech Phys Solids 95:284–307

[54] Cui S, Wan J, Zuo X, Chen N, Rong Y (2016) Interface stress evolution of martensitic transformation in MnCu alloys: a phase-field study. Mater Design 109:88–97

[55] Denoual C, Vattré A (2016) A phase field approach with a reaction pathways-based potential to model reconstructive martensitic transformations with a large number of variants. J Mech Phys Solids 90:91–107

[56] Toloui M, Militzer M (2018) Phase field modeling of the simultaneous formation of bainite and ferrite in TRIP steel. Acta Mater 144:786–800

[57] Levitas VI, Javanbakht M (2014) Phase transformations in nanograin materials under high pressure and plastic shear: nanoscale mechanisms. Nanoscale 6(1):162–166

[58] Levitas VI, Javanbakht M (2015) Interaction between phase transformations and dislocations at the nanoscale. Part 1. General phase field approach. J Mech Phys Solids 82:287–319

[59] Levitas VI, Javanbakht M (2015) Interaction between phase transformations and dislocations at the nanoscale. Part 2: phase field simulation examples. J Mech Phys Solids 82:164–185

[60] Javanbakht M, Levitas VI (2016) Phase field simulations of plastic strain-induced phase transformations under high pressure and large shear. Phys Rev B 94:214104

[61] Javanbakht M, Levitas VI (2018) Nanoscale mechanisms for high-pressure mechanochemistry: a phase field study. J Mater Sci 53(19):13343–13363. https://doi.org/10.1007/s10853-018-2175-x

[62] Levitas VI, Preston DL (2002) Three-dimensional Landau theory for multivariant stress induced martensitic phase transformations. II. Multivariant phase transformations and stress space analysis. Phys Rev B 66:134207

[63] Clapp PC, Besquart CS, Shao Y, Zhao Y, Rifkin JA (1994) Transformation toughening explored via molecular dynamics and Monte Carlo simulations. Modell Simul Mater Sci Eng 2:551–557

[64] Wang Y, Liu ZK, Chen LQ (2004) Thermodynamic properties of Al, Ni, NiAl, and Ni3Al from first-principles calculations. Acta Mater 52:2665–2671

[65] Wang C, Xu J, Hu X, Chen D, Sun H, Yu B (2011) Elastic and thermodynamic characteristics of NiAl and Ni3Al from first-principles calculations. Int J Mod Phys B 25:3623–3631